NEUROSCIENCE

A nasal chemosensation–dependent critical window for somatosensory development

Linbi Cai[1,2], Ali Özgür Argunşah[1,2], Angeliki Damilou[1,2], Theofanis Karayannis[1,2,3]*

Nasal chemosensation is considered the evolutionarily oldest mammalian sense and, together with somatosensation, is crucial for neonatal well-being before auditory and visual pathways start engaging the brain. Using anatomical and functional approaches in mice, we reveal that odor-driven activity propagates to a large part of the cortex during the first postnatal week and enhances whisker-evoked activation of primary whisker somatosensory cortex (wS1). This effect disappears in adult animals, in line with the loss of excitatory connectivity from olfactory cortex to wS1. By performing neonatal odor deprivation, followed by electrophysiological and behavioral work in adult animals, we identify a key transient regulation of nasal chemosensory information necessary for the development of wS1 sensory-driven dynamics and somatosensation. Our work uncovers a cross-modal critical window for nasal chemosensation–dependent somatosensory functional maturation.

The sensory experiences of neonatal mammals diverge substantially from those of adults, given the asynchronous and varied maturation of their sensory systems before reaching full functionality (*1*–*3*). In mammals, it has been shown that olfaction is not only the evolutionarily oldest, but also the first sensory modality to mature, allowing the detection of odor stimulants already in the womb (*4*, *5*). This odor information is essential for neonatal well-being and survival (*6*–*8*), largely traveling via the main olfactory pathway, which bypasses the thalamus, to activate the cortex in a nontopographic manner (*9*–*12*). Beyond the main olfactory pathway, different odors can also engage the vomeronasal organ, the Grueneberg ganglion, the septal organ of Masera, or even the nasal trigeminal system, which are all well-operating after birth (collectively comprising nasal chemosensation) (*13*, *14*).

Together with nasal chemosensation, somatosensation is also functional at birth (*15*–*17*), and it is only at around postnatal day (P) 11 and P14 that mice begin processing external auditory and visual information, respectively (*18*–*22*). Therefore, nasal chemosensation and somatosensation work in tandem to allow neonates to perceive the world (*7*, *16*, *23*) and also cross-modally regulate other senses to affect adult behavior (*23*–*25*). In adult mice, cross-modal integration is primarily performed in higher-order cortical areas (*26*, *27*) and to a smaller extent in primary sensory areas (*28*–*31*). In this study, we postulated that nasal chemosensation might have a stronger influence on cortical activity—and on the somatosensory system—before other sensory modalities contribute to multisensory processing and before higher-order cortical areas are incorporated in circuit dynamics.

[1]Laboratory of Neural Circuit Assembly, Brain Research Institute (HiFo), University of Zurich, Winterthurerstrasse 190, CH-8057 Zurich, Switzerland. [2]Neuroscience Center Zurich, Winterthurerstrasse 190, CH-8057 Zurich, Switzerland. [3]University Research Priority Program (URPP), Adaptive Brain Circuits in Development and Learning (AdaBD), University of Zurich, CH-8057 Zurich, Switzerland.
*Corresponding author. Email: karayannis@hifo.uzh.ch

Odor-evoked information propagates to the wS1 in neonatal mice

Although it is known that in adult mice, odor information propagates from the olfactory bulb (OB) to the olfactory cortex (*32*), its routing in neonatal mice is unknown. We therefore first investigated the progression of odor-evoked activity in the dorsal cortex—also focusing on the primary somatosensory area—before and after auditory and visual information engage the cortex. We performed acute transcranial wide-field calcium imaging experiments at P3 to P7 and P23 to P40 in mice expressing the calcium indicator (GCaMP6) in all brain neurons under the synaptosomal-associated protein 25 (*Snap25*) promoter (*Snap25-2A-GCaMP6-D* mice). Just air or an odor (2-heptanone or peppermint; see supplementary text for more information on odors) was delivered to the mouse's nostrils with a custom-built odor delivery system (*33*) (Fig. 1A). By measuring the change in fluorescence of the calcium indicator (ΔF/F) and subtracting the control air-puffing activity from the odor-puffing activity, we found that the odor information propagated to a large part of the cortex in the neonates but only to restricted regions in adult mice (Fig. 1B and fig. S1A). When analyzing the signal in the primary whisker somatosensory cortex (wS1), we found that the odor led to its activation in neonates (Fig. 1C and fig. S1B), whereas in adult mice it had an inhibitory effect (Fig. 1D). To assess the type of activity recorded with the calcium imaging, we performed in vivo multielectrode recordings simultaneously in the OB and wS1 using the same odor-stimulation paradigm (Fig. 1E). We first aligned the odor-evoked activity in both recorded regions to the first peak of breathing (inhalation) using trial-by-trial data collection (fig. S1C). The different cortical layers in wS1 were identified by analyzing the local field potential (LFP) and the current source-density (CSD) profile upon whisker stimulation (Fig. 2F). We then measured the wS1 activity for 1 s, which includes approximately two breathing cycles. We found that odor itself, but not air, led to a sink in the LFP—and hence excitation in wS1 in neonatal mice—without evoking spiking activity (Fig. 1, F and G). By contrast, there was no difference in either LFP or multiunit activity (MUA) between air puffing and odor stimulation in any of the layers of wS1 in adult animals (fig. S1, D and E). These results largely agree with the wide-field calcium imaging data and indicate that nasal chemosensory information propagates to wS1 in neonates, inducing subthreshold activation, a phenomenon not present in adult mice.

Odor-evoked information enhances wS1 whisker-evoked activity in neonatal mice

We next explored the effect of odor stimuli on whisker-evoked activity in wS1 because the effect we observed from odor-only stimulation in wS1 was subthreshold. Basing our approach on the timing of reaching peak activity in wS1 and in order to simulate a naturalistic scenario in which neonatal mice first smell the odor of the mother or siblings, for example, (*34*–*37*) and then navigate toward them using the whisker system (*36*, *38*), we delivered the odor stimulus 2 s before the whisker stimulation (Fig. 2, A and E). Wide-field calcium imaging in neonatal mice showed that the combined odor-whisker sensory stimulation evoked significantly higher calcium activity in wS1 ($P = 0.0039$) compared with the effect when deflecting the whiskers alone (air flowing with multi-whisker stimulation) (Fig. 2, B and C, and fig. S2, A and B). In addition, the odor–multi-whisker (Odor+W) ΔF/F amplitude was significantly higher ($P = 0.0078$) than the sum of the air–multi-whisker (Air+W) ΔF/F amplitude and the odor-only ΔF/F amplitude (fig. S2C). This supralinear odor-enhancement effect (OEE) suggested that the same group of neurons in wS1 process the odor and whisker information in the neonates. To look at the OEE process in more depth, we performed silicon-probe recordings in wS1 at P3 to P7 in anesthetized and awake mice after applying the same odor- and whisker-stimulation protocols (Fig. 2E). Analysis of the MUA in wS1 revealed that the odor stimulation enhanced the whisker-evoked activity in layer (L) 2-3 and L4 in neonates (Fig. 2, G and H, and fig. S2, E and F). Furthermore, the OEE was observed for both peak amplitude and whole poststimulation activity (2 s) in L2-3 of the neonatal cortex, whereas it was not evident in the peak amplitude in L4 wS1 (Fig. 2, G and H, and fig. S2, E and F). Spike sorting showed that 18% of L2-3 responding neurons and 17% of L4

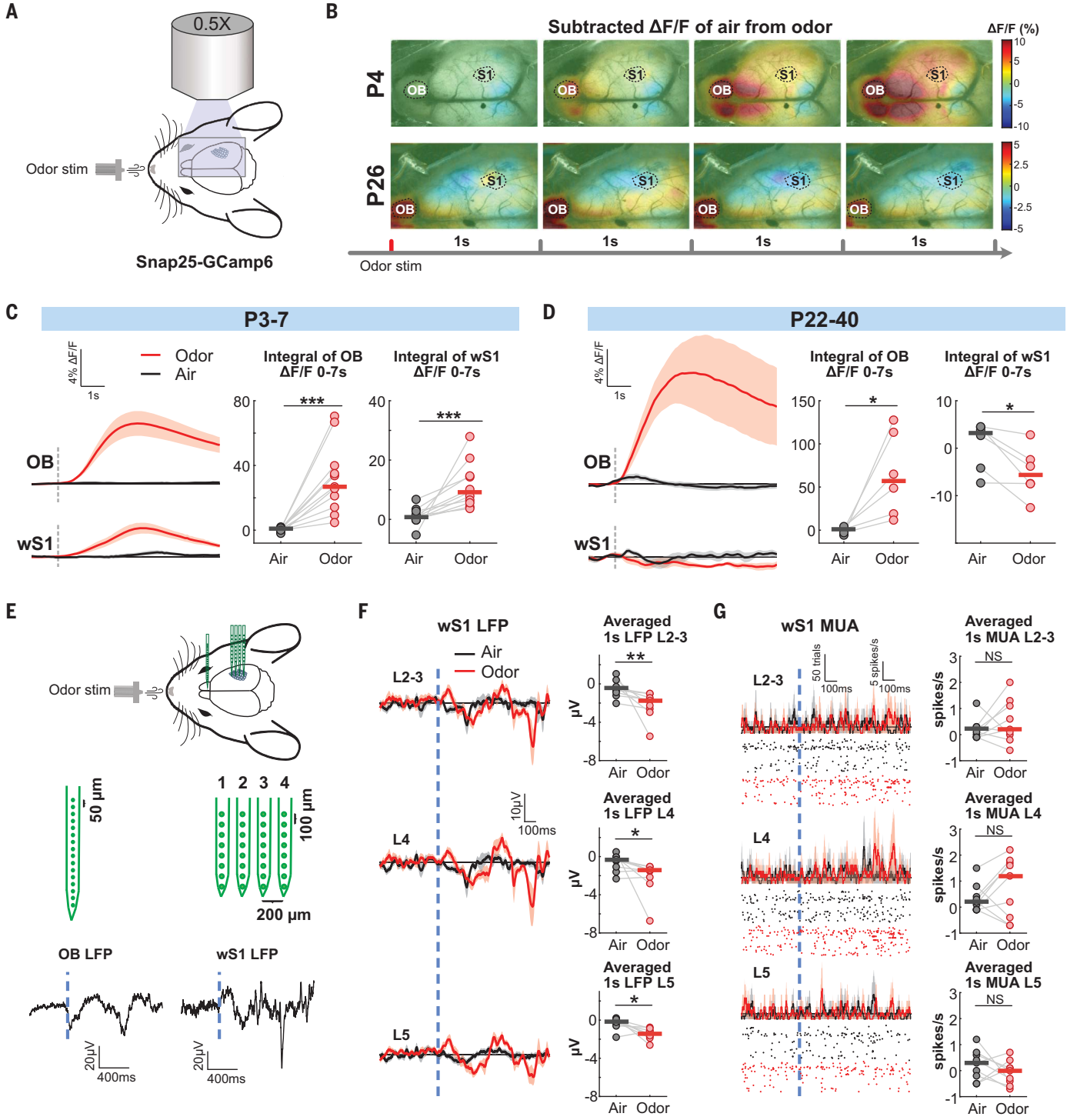

Fig. 1. The propagation of the nasal chemosensory information to the cortex in neonatal and adult mice. (**A**) Experiment design showing wide-field calcium imaging of Snap25-GCamp6 mice. (**B**) Subtracted ΔF/F of air flowing from odor stimulation in a P4 and a P26 mouse upon odor delivery. (**C** and **D**) (Left) Temporal profile of the averaged calcium responses in OB and wS1 with air flowing (black) and odor (2-heptanone or peppermint) delivery (red) at P3 to P7 (C) and P23 to P40 (D). (Right) Area under the curve (AUC) of ΔF/F in the OB and wS1 for 7 s after the onset of the air flowing (black) or odor stimulation (red) at P3 to P7 (n = 11 mice) (C) and P23 to P40 (n = 6 mice) (D). (**E**) (Top) Experiment design showing multielectrode recording in OB and wS1. (Bottom) Example traces of P6 mouse OB and wS1 L2-3 local field potential (LFP) after the onset of the odor stimulation. (**F**) (Left) Averaged LFP in P3 to P7 mice wS1 L2-3, L4, and L5 (n = 9 shanks from N = 5 mice) after the onset of air flowing (black) and odor stimulation (red). (Right) Averaged LFP for 1 s after the onset of air flowing (black) or odor stimulation (red). (**G**) (Left) Grand average and scatter plot of MUA recorded in P3 to P7 mice (n = 9 shanks from N = 5 mice) wS1 after the onset of air flowing (black) and odor stimulation (red). (Right) Averaged MUA for 1 s after the onset of air flowing (black) or odor stimulation (red). Black and red lines in (C), (D), (F), and (G) indicate the median of the group in each plot, and the shading indicates the SEM. NS, not significant, $P > 0.05$, *$P < 0.05$, **$P < 0.01$, ***$P < 0.001$.

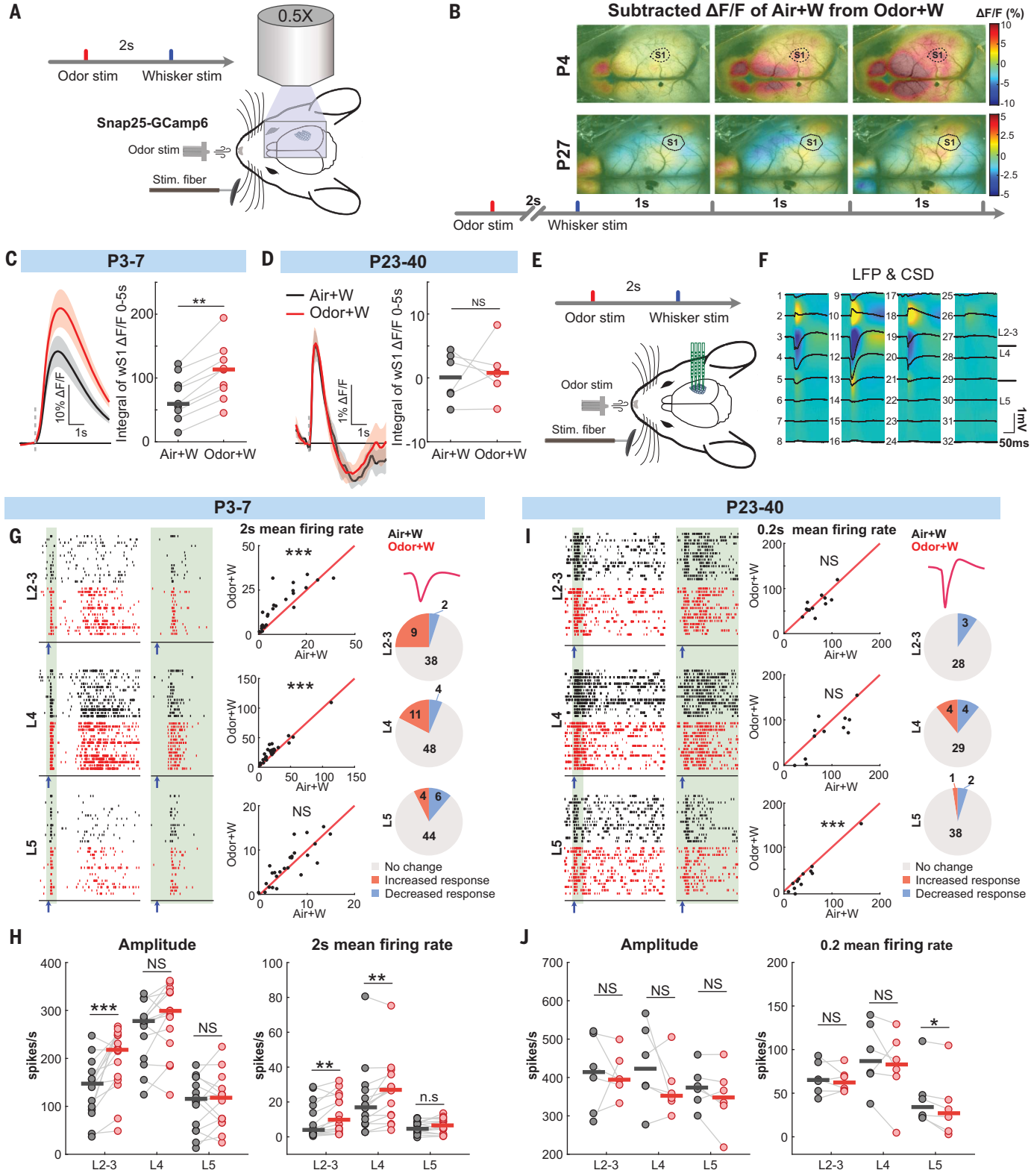

Fig. 2. The odor stimulation enhances wS1 whisker-evoked activity in neonatal mice. (**A**) Experimental design. (**B**) Subtracted ΔF/F of Air+W stimulation from Odor+W stimulation in a P4 and a P27 mouse upon whisker stimulation. (**C** and **D**) (Left) Temporal profile of calcium imaging average responses recorded in wS1 after Air+W stimulation (black) versus Odor+W stimulation (red) at P3 to P7 (n = 9 mice) and P23 to P40 (n = 6 mice). (Right) AUC of ΔF/F in wS1 comparing Air+W stimulation and Odor+W stimulation at P3 to P7 (C) and P23 to P40 (D). (**E**) Experimental design. (**F**) Example of evoked LFP response and CSD plots elicited by Odor+W stimulation. (**G** and **I**) (Left) Raster plot of a P7 (G) and a P26 (I) mouse wS1 L2-3, L4, and L5 MUA responses after Air+W (black) stimulation versus Odor+W (red) stimulation during 2 s. The shaded window shows the detailed spiking activity during the period of 200 ms upon whisker stimulation (blue arrow). (Middle) Scatter plots of all recording positions in wS1 L2-3, L4, and L5 of P3 to P7 groups (n = 27 shanks out of N = 15 mice) and P23 to P40 groups (n = 12 shanks out

of N = 6 mice) evoked MUA mean firing rate (spikes/s) of 2 s (P3 to P7) or 200 ms (P23 to P24) to Air+W stimulation versus Odor+W stimulation. (Right) Pie charts of neurons do not change, increase, or decrease their spiking activity upon 2 s (P3 to P7) or 200 ms (P23 to P40) when comparing Odor+W stimulation with Air+W stimulation. (**H**) Peak amplitude of P3 to P7 mice (n = 15 mice) wS1 L2-3, L4, and L5 and evoked MUA mean firing rate (spikes/s) of 2 s (n = 15 mice) of L2-3, L4, and L5 upon whisker stimulation. (**J**) Peak amplitude of P23 to P40 mice (n = 6 mice) and evoked MUA mean firing rate (spikes/s) of 200 ms (n = 6 mice) of wS1 in all layers after stimulation. Black and red lines indicate the median of the group in each plot. The shading in (C) and (D) indicates the SEM. NS, $P > 0.05$, *$P < 0.05$, **$P < 0.01$, ***$P < 0.001$.

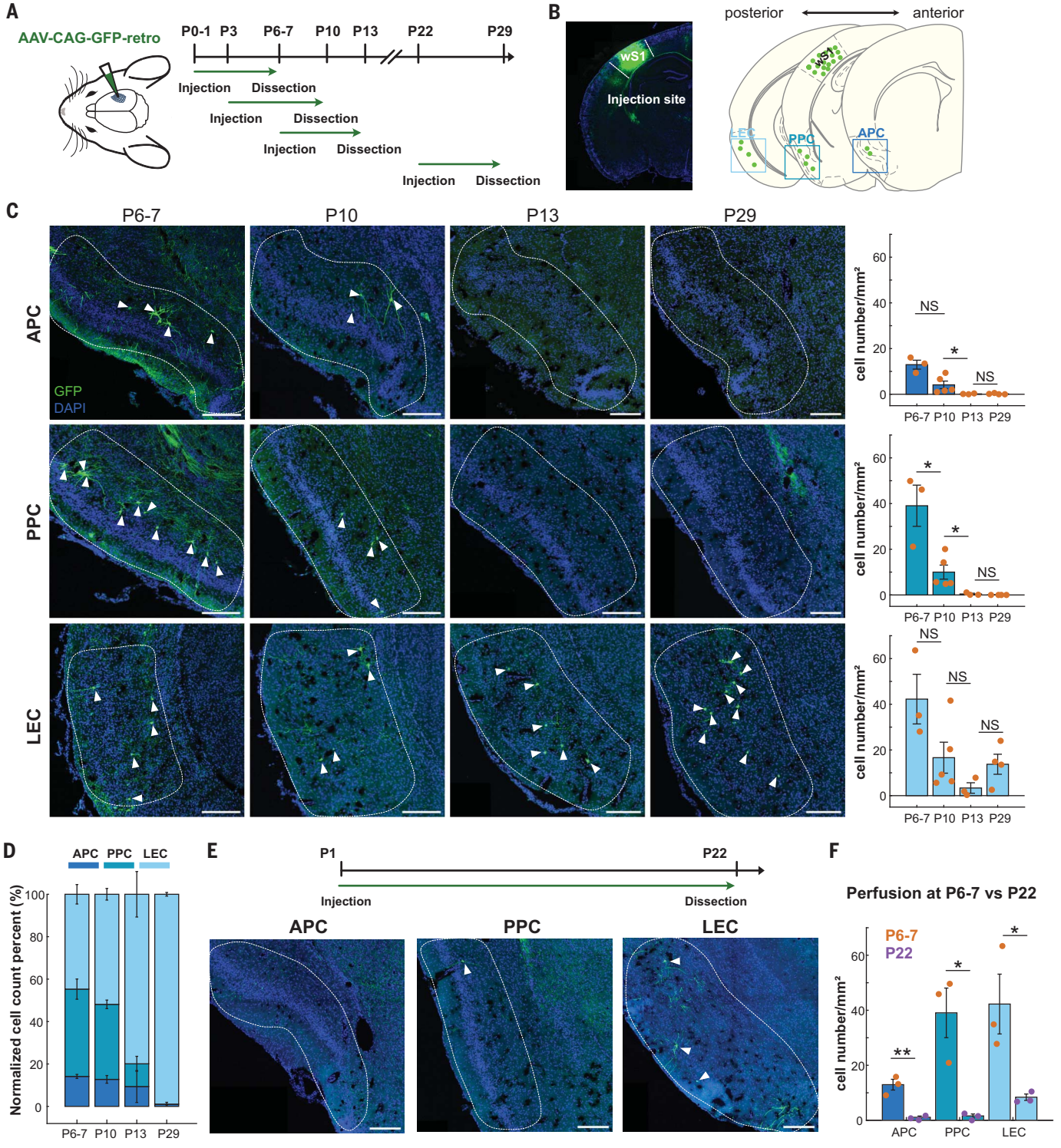

Fig. 3. wS1 receives transient inputs from the piriform cortex during development. (**A**) Schematic showing AAV injections in wS1 at different ages (P0 to P1, P3, P7, and P22) and brain dissections 6 to 7 days after the virus injection. (**B**) An example image of the virus injection site and the schematic coronal sections depicting detected neurons in APC, PPC, and LEC. (**C**) (Left) Examples of GFP-labeled neurons in APC, PPC, and LEC at different ages (P6 to P7, P10, P13,

and P29). Scale bars, 200 μm. (Right) Quantification of GFP-labeled cell numbers in APC, PPC, and LEC at different ages (P6 to P7: n = 3; P10: n = 5; P13: n = 3; P29: n = 4). (**D**) Mean percentage of cell number in APC, PPC, and LEC averaged over each mouse at different ages. (**E**) (Top) Schematic representation of the AAV-CAG-GFP-retro injection at P1 and dissection at P22. (Bottom) Examples of GFP-labeled neurons in APC, PPC, and LEC after 3 weeks postinjection survival and development. Scale bars, 200 μm. (**F**) Quantification of GFP-labeled neuron number/mm^2 at P6 to P7 (injected at P0 to P1) and P22 (injected at P1) (n = 3 mice at each group). Error bars in (C), (D), and (F) indicate SEM. NS, $P > 0.05$, $^*P < 0.05$, $^{**}P < 0.01$.

responding neurons increased their firing rate in Odor+W, whereas only 4% of L2-3 neurons and 6% of neurons decreased their responses in neonates (Fig. 2G). In adult mice aged P23 to P40, wide-field calcium imaging and silicon-probe recordings did not show OEE in wS1, but we observed an inhibitory effect in the L5 late-spiking phase (Fig. 2, B, D, I, and J, and fig. S2D). In line with the MUA findings in adult animals, spike-sorting analysis showed that more neurons are down-regulated by Odor+W stimulation as compared with Air+W stimulation (Fig. 2I). Overall, our experiments show that in the first postnatal week of mice, odor-induced activity reaches wS1 and enhances its whisker-evoked activation. This excitatory cross-modal odor-whisker interaction was transient and was not observed in adult mice.

Transient developmental connections between olfactory and somatosensory wS1 cortex

We subsequently investigated the underlying basis for the transient OEE, focusing on potential long-range connections between the olfactory cortex and wS1 in neonates, which would disappear during development. To probe for these connections, we injected a retrograde adeno-associated virus (AAV-CAG-EGFP-retro) in wS1 and assessed incoming connectivity at the two developmental time points examined functionally, P3 to P7 and P23 to P40 (Fig. 3, A and B) (EGFP, enhanced green fluorescent protein). After injecting the AAV in wS1 at P0 to P1 and analyzing the tissue at P6 to P7, we observed GFP-labeled neurons in the olfactory cortex [anterior piriform cortex (APC), posterior piriform cortex (PPC), and lateral entorhinal cortex (LEC)] (Fig. 3C). By contrast, when performing the same injections of the retrograde AAV in adult mice, we observed no fluorescently labeled neurons in the APC or PPC and only a small number in LEC (Fig. 3C). The results in adult animals are consistent with the published literature (*39*). To examine the time course of the loss of these connections, we injected the virus in wS1 at P3 and P7 and then analyzed the tissue at P10 and P13, respectively (Fig. 3A). Fewer GFP-positive neurons were found in the piriform cortex (APC and PPC) at P10 and even fewer at P13. (Fig. 3C). By normalizing the cell numbers in each of these three different regions to the neurons observed in all of them, we found that the percentage of the neurons in the piriform cortex (APC and PPC) drastically dropped to almost zero from the first postnatal week to adult (from 14.13 to 1.07% in APC and from 41.16 to 0% in PPC). The normalized data also show that the percentage of neurons in the LEC shifted in the opposite direction with age and increased from 44.71 to 98% (Fig. 3D). Therefore, the piriform cortex undergoes the biggest change in terms of connectivity to wS1 during the first 3 postnatal weeks. Due to the fast changes in the developing brain and the relatively long waiting period (6 to 7 days) for viral expression, we also repeated the connectivity mapping with a faster retrograde chemical dye tracer for better time resolution (fig. S3). The results show that the connections from piriform to wS1 were gone by P15 (fig. S3, B and C). Overall, the tracing results show that the long-range connections from the piriform cortex to wS1 are present in the first postnatal week and disappear around the end of the second postnatal week. By contrast, connections from LEC to wS1 remain across the ages tested.

We subsequently examined whether the progressive loss of connectivity from the piriform cortex to wS1 is due to developmental axonal trimming or cell death in the piriform cortex. To assess this, retrograde AAV-GFP or fluorogold was injected in wS1 at P1 and P4, and the mice were sacrificed at P22 and P26, respectively (Fig. 3E and fig. S3D). Analysis of the tissue at these time points showed a decrease of neuron numbers in all olfactory cortical regions (Fig. 3F). These results suggest that the developmental loss of connectivity is due to developmental cell death of the wS1-projecting piriform neurons in the first 2 postnatal weeks rather than the loss of axonal connections alone.

Acute silencing of olfactory cortex activity abolishes OEE in neonates

Because we observed direct long-range connectivity from the piriform cortex to wS1, we next assessed the type of neurons that are providing it. It has been shown that within the first postnatal week, γ-aminobutyric acid–releasing (GABAergic) neurons can induce excitation rather than inhibition, owing to the absence of the membrane transporter KCC2 and the difference in the chloride concentration gradient (*40*). By injecting fluorogold in wS1 at P3 in mice expressing tdTomato in all the GABAergic neurons (*Dlx6Cre-Ai14* line) and analyzing the tissue at P7, we found that none of the fluorogold-positive neurons in the piriform cortex co-label with tdTomato. This indicates that the wS1-projecting neurons in the piriform cortex are non-GABAergic (Fig. 4, A and B).

In the absence of long-range GABAergic neurons mediating the OEE through potential excitatory actions, we next tested for the involvement of local wS1 GABAergic neurons underlying neonatal OEE. To investigate whether the actions of GABA on wS1 neurons are involved in the OEE, we applied a $GABA_A$ receptor antagonist (gabazine) in wS1 of P3 to P7 mice while performing silicon-probe recordings and multisensory stimulation as before (Fig. 4C). The application of gabazine increased whisker-evoked activity upon whisker stimulation alone in wS1 but did not abolish OEE either in L2-3 or L4 (Fig. 4, D and E). These results indicate that $GABA_A$ receptors mediate an overall inhibitory effect in vivo in the first postnatal week in wS1 and do not underlie the observed OEE in neonatal mice. Our experiments therefore suggest that excitatory inputs from glutamatergic piriform neurons to wS1 may be the key to OEE.

After confirming the engagement of PPC in odor processing in neonates anatomically and functionally (supplementary text) (fig. S4, A to F), we tested the functionality and type of piriform-wS1 connections by injecting AAV-syn-ChR2-mCherry in the piriform cortex of newborn mice (P0 to P1). We recorded L2-3 wS1 pyramidal neurons at P6 to P8 in whole-cell patch-clamp mode in vitro (Fig. 4, F and G) because these cells showed consistent OEE in both whisker-evoked amplitude and mean firing rate. By shining blue light to evoke neurotransmitter release from the Ch2R-labeled fibers coming from wS1-projecting piriform neurons and holding the membrane potential at −70 mV, we observed excitatory glutamatergic responses in L2-3 pyramidal neurons, but we failed to see any inhibitory synaptic input when holding the cells at 0 mV (Fig. 4G and fig. S4, G to I). These results are in line with the gabazine in vivo experiments and indicate that wS1 L2-3 pyramidal cells receive transient direct excitatory glutamatergic input from the piriform cortex in the first postnatal week, and this correlates with the OEE in neonates.

Lastly, we aimed to determine whether the activation of the direct excitatory pathway between piriform and wS1 underlies OEE in the neonates in vivo. We therefore performed silicon-probe recordings in wS1 in neonates, before and after acutely silencing the PPC by injecting tetrodotoxin (TTX) to block action potentials (Fig. 4H). Indeed, we found that upon TTX application in the PPC of neonatal mice, wS1 L2-3 odor–whisker-evoked responses decreased as compared with the responses before TTX application (Fig. 4, I and J). These results suggest

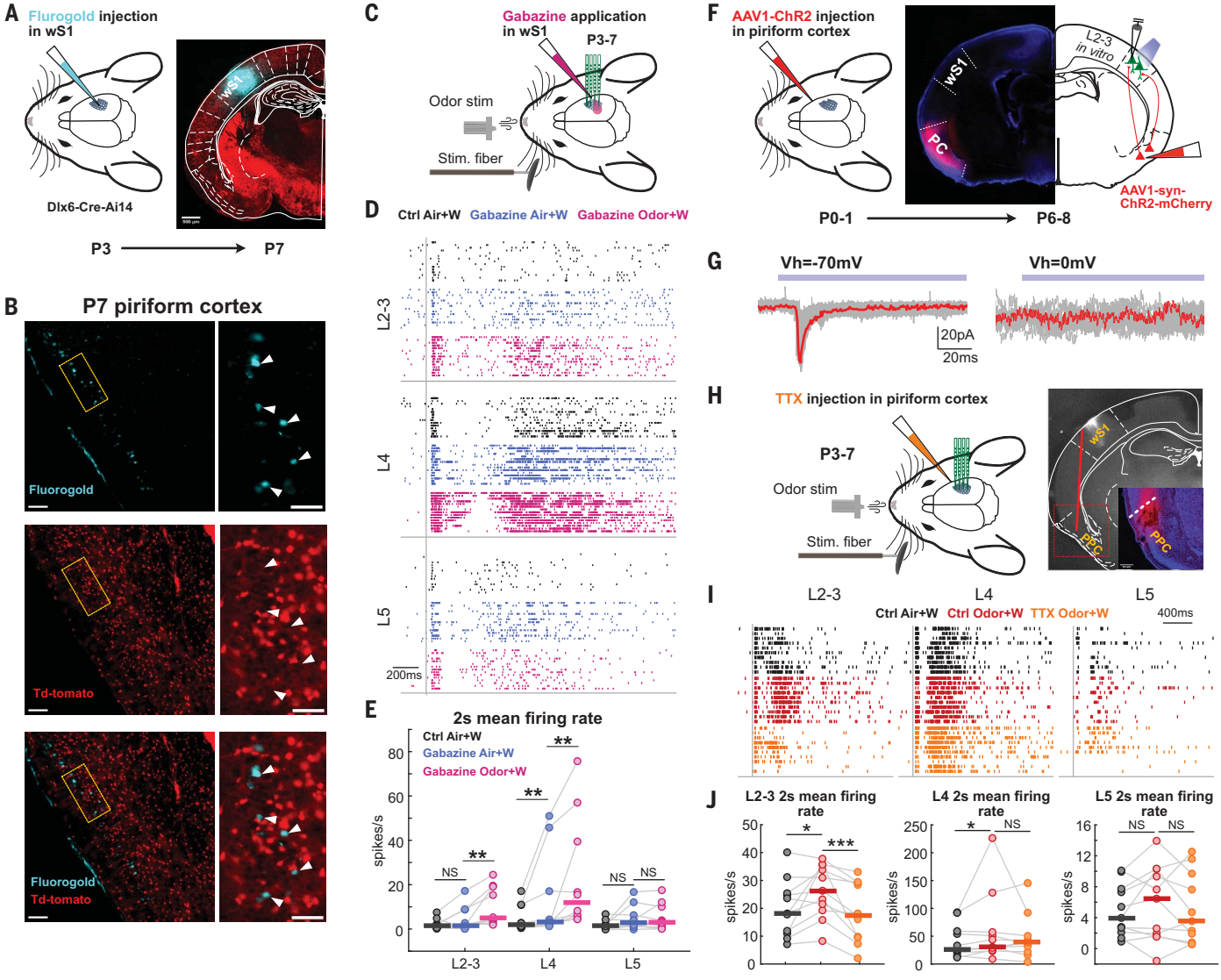

Fig. 4. The excitatory input from the piriform cortex is responsible for the odor-enhancement effect in wS1 of neonatal mice. (**A**) (Left) A schematic of fluorogold injections at P3 and tissue process at P7. (Right) An example of the injection site of a P7 brain. (**B**) (Left) Example images of fluorogold-positive neurons in the piriform cortex. Single-channel images with fluorogold (cyan) and td-tomato (red) and merged channel. (Right) Rectangular panels are enlarged images of the boxed areas on the left. Scale bar, 200 μm (left panels), 50 μm (right zoom-in panels). (**C**) A schematic showing gabazine application on the wS1 while performing the silicon-probe recording. (**D**) Raster plots of a P6 mouse MUA activity in wS1 L2-3, L4, and L5 during 2 s upon Air+W stimulation in the control condition (black), Air+W stimulation with gabazine (blue), and Odor+W stimulation with gabazine (magenta) (n = 10 from N = 4 mice). (**E**) Mean firing rate of wS1 all layers during 2 s upon whisker stimulation among three conditions. Black, blue, and magenta lines indicate the median of each data group. (**F**) An illustration of the AAV injections in the piriform cortex at P0 to P1 and conducting the in vitro patch clamp in wS1 L2-3 pyramidal neurons at P6 to P8 with blue-light photon stimulation. (**G**) Example traces of the blue-light–induced evoked inhibitory postsynaptic current (IPSC) and excitatory postsynaptic current (EPSC) in a wS1 L2-3 pyramidal neuron. Vh, holding potential. (**H**) (Left) A schematic showing silencing of the piriform cortex by injection of TTX while silicon-probe recording in P3 to P7 mice. (Right) An example histological image from an in vivo recorded brain reconstructing the DiI-labeled silicon-probe trace (white) in wS1 and microglass pipette trace (red) containing TTX reaching the piriform cortex. (Inset) Zoom-in of the inserted piriform cortex (red box). (**I**) Raster plots of wS1 evoked MUA responses in all layers after inserting the capillary without injecting the TTX upon Air+W stimulation (black) and Odor+W stimulation (red) and after injecting TTX upon Odor+W stimulation (orange). (**J**) Mean firing rate of wS1 in all layers during 2 s upon whisker stimulation in three conditions (n = 10 from N = 4 mice). Black, red, and orange lines indicate the median of each group. NS, $P > 0.05$, $^{*}P < 0.05$, $^{**}P < 0.01$, $^{***}P < 0.001$.

that the direct piriform-wS1 glutamatergic inputs drive OEE in neonatal wS1.

Neonatal odor deprivation leads to somatosensory defects in adult mice

Our experiments uncovered a previously unknown transient anatomical and functional interaction from the olfactory cortex to the somatosensory system of mice, which is lost around P14. We next investigated the importance of this early interaction for the development of wS1 by depriving one hemisphere of newborn mice of nasal chemosensory information at P0 to P1 by unilateral nostril occlusion. After verifying that the manipulation was effective (fig. S6A), we performed silicon-probe recordings in wS1 of adult mice after single-whisker stimulation. Because we had observed a modulating role of odors to whisker-driven activity in neonatal wS1, we designed our experiments to reveal the overall

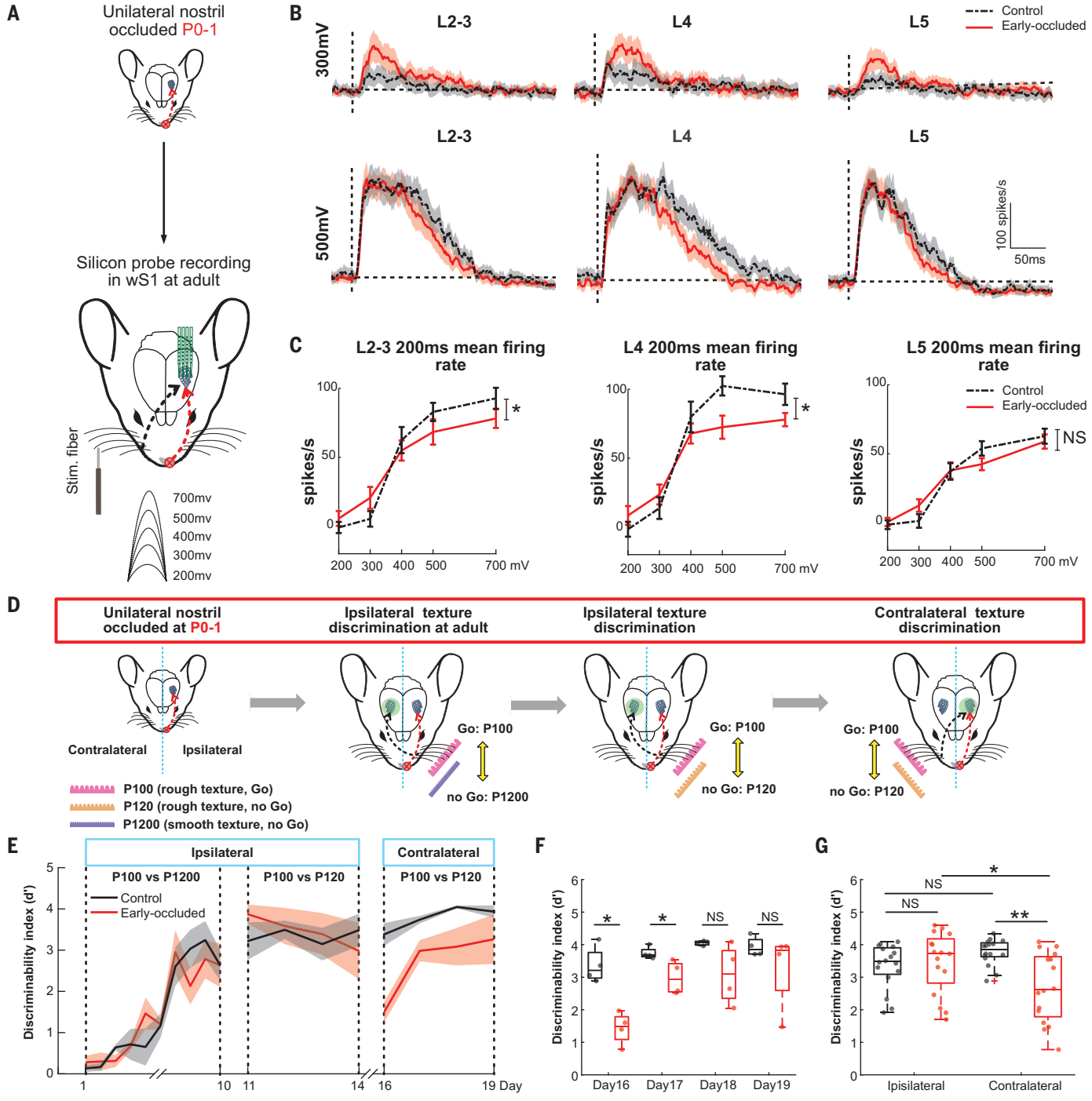

Fig. 5. Odor deprivation at an early age narrows neural dynamic range in wS1 and leads to texture discrimination deficiency. (**A**) Schematic illustration showing the single nostril occluded at P0 to P1 and performance of the silicon-probe recording in the barrel cortex with various strengths of single-whisker stimulation in adults (P24 to P57). (**B**) Grand average traces of evoked L2-3, L4, and L5 MUA responses upon the different strengths of single-whisker stimulation in P0 to P1 nostril-occluded mice (red, n = 13 barrels from 5 mice) and littermate control mice (black, n = 13 barrels from 5 mice). (**C**) Input-output plot of 200-ms mean firing rate for different strengths of whisker stimulation (200 to 700 mV) in L2-3, L4, and L5. (**D**) Experimental design for texture-discrimination task. Early-occluded mice and control mice were trained on the ipsilateral whiskers of the occluded nostril to distinguish between a rough sandpaper (P100 grit) serving as a target stimulus (Go), and a smooth sandpaper (P1200 grit) serving as a nontarget stimulus (No-Go). After becoming the expert at the task, the mice needed to distinguish between the Go (P100) and a slightly less-rough texture (P120 grit), which also served as a No-Go target. Afterward, they performed the task of distinguishing P100 versus P120 by the contralateral whiskers to examine the performance of the odor-deprived wS1. (**E**) Averaged learning curve based on the discriminability index (d′) in control and early-occluded mice. (**F**) Group comparison of d′ after switching to the contralateral side of the whiskers in control (n = 4) and early-occluded mice (n = 4) day-by-day starting from the expert performance of control. (**G**) Group comparison of d′ with ipsilateral whiskers and contralateral whiskers in control and early-occluded group. The shading in (B) and (E) indicates the SEM; the error bar in (C) indicates the SEM; and box plots show the medians with the interquartile range (box) and range (whiskers). NS, $P > 0.05$, *$P < 0.05$, **$P < 0.01$.

dynamics of neural responses using various whisker-stimulation strengths (Fig. 5A). By measuring the 200-ms mean firing rate after single-whisker stimulation at each strength, we found that early (P0 to P1)–occluded mice displayed a smaller neural dynamic range in wS1 upper layers (L2-3 and L4) as compared with control animals (Fig. 5, B and C). Spike-sorting showed that in L2-3, the individual neuron's firing rate was not statistically different among various stimulation strengths, but when the firing rate was multiplied by the neuronal probability rate, the overall neural network had a lower dynamic range (fig. S5, B and C). This result indicates that the smaller neural dynamic range in early occluded mice in wS1 L2-3 is likely due to a lower response probability to whisker stimulation of individual neurons (fig. S5, A to C). However, for wS1 L4, both neuronal spiking rate and spiking probability of individual neurons accounted for the smaller dynamic range that we observed (fig. S5, A to C). These results demonstrate that nasal chemosensory information early in life is important to set the proper whisker-driven neural dynamic spiking range of wS1 upper layers.

On the basis of these results, we tested whether early-occluded adult mice, exhibiting a smaller neural dynamic range, might display difficulties in texture discrimination, especially when items with close statistics are presented. We therefore examined the tactile acuity of awake-behaving, head-restrained early-occluded and control adult mice through a go–no-go whisker-based texture discrimination task (Fig. 5D). We first ruled out learning deficiency in early-occluded mice by training them to differentiate two sandpapers of substantially different granularity [rough: P100 grit (Go); smooth: P1200 grit (No-Go)] ($d' > 1.5$), followed by two close textures (rough: P100 grit (Go); smooth: P120 grit (No-Go)] on the ipsilateral side of the nostril occlusion, which corresponds to the unaffected wS1 (Fig. 5E). Subsequently, we switched the task and presented the textures on the contralateral side of the nostril occlusion, where the corresponding wS1 was affected by the early nostril occlusion (Fig. 5D). Whereas control mice performed the texture discrimination task similarly well on both sides of the whiskers, early-occluded mice performed much worse compared with controls when using the manipulated side (Fig. 5, E to G). Furthermore, a comparison between the ipsilateral and contralateral whisker performance revealed that control mice performed equally well with both sides, whereas early-occluded mice performed worse when using contralateral whiskers, which transmit information to the odor-deprived wS1 (Fig. 5G) (supplementary text).

Our anatomical results showed the disappearance of the transient piriform-to-wS1 connections by P15. To test that the observed sensory discrimination phenotype was due to the loss of nasal chemosensory input during the first 2 postnatal weeks, we performed the same experiments in mice that had been unilaterally occluded at P15 to P16. We found no difference in their texture-discrimination abilities, whether using ipsilateral or contralateral whiskers, except for a slightly slower learning curve compared with control mice (fig. S6, C to E). In contrast to earlier occlusion, there was also no performance difference between ipsilateral and contralateral whiskers for late-occluded mice (fig. S6F). These behavioral results indicate that early neonatal—but not late—odor deprivation can lead to somatosensory discrimination deficits. Our findings overall indicate a crucial role of transient developmental inputs from the nasal chemosensory system to the somatosensory cortex for the proper maturation of the latter.

Discussion

Even though nasal chemosensation is understood to be a distinctive early system in humans and rodents, little is known about how it interacts with other sensory modalities across development. We have discovered that nasal chemosensation and somatosensation interact strongly through transient connectivity between the olfactory and somatosensory primary cortical areas before the full set of senses develops and that this is key for the developmental acuity of somatosensation.

Both odorants tested in this study stimulate not only olfactory pathways but can also engage intra- or extranasal trigeminal receptors in a concentration-dependent manner (*41*–*43*). Therefore, in our current experimental design, we cannot tease apart the potential contribution of nonolfactory odor-driven brain activation, and further investigation is needed to distinguish such components.

Regardless, the transient connectivity from the piriform cortex to wS1 starts to decrease when auditory stimuli begin to drive cortical activity (~P11) and disappears by the time mice open their eyelids and detailed visual stimuli engage the cortex (~P14). The profound anatomical and functional changes we have observed suggest a drastic shift in multisensory processing throughout development, from an expanded cortical network in neonates to more specialized higher-order cortical areas in adults. Although it is not known whether similar processes take place in the human brain, an influence of nasal chemosensation on somatosensation has also been reported in people with congenital or acquired anosmia with changes in receptive fields, chemosensory threshold detection, and somatosensory cortical activity (*44*–*50*).

Overall, our study reveals the existence of dynamic developmental cross-modal interactions in the mammalian brain and suggests that nasal chemosensation has a priming role in the maturation of sensory processing.

REFERENCES AND NOTES

1. S. N. Graven, J. V. Browne, *Newborn Infant Nurs. Rev.* **8**, 169–172 (2008).
2. M. S. Grubb, I. D. Thompson, *Curr. Opin. Neurobiol.* **14**, 503–512 (2004).
3. R. Lickliter, *Clin. Perinatol.* **38**, 591–603 (2011).
4. B. Schaal, T. Hummel, R. Soussignan, *Clin. Perinatol.* **31**, 261–285 (2004).
5. Y. N. Chen, J. K. Kostka, S. H. Bitzenhofer, I. L. Hanganu-Opatz, *Curr. Biol.* **33**, 4353–4366.e5 (2023).
6. D. W. Logan *et al*., *Curr. Biol.* **22**, 1998–2007 (2012).
7. C. Raineki *et al*., *Braz. J. Med. Biol. Res.* **43**, 914–919 (2010).
8. S. S. Miller, N. E. Spear, *Dev. Psychobiol.* **51**, 488–504 (2009).
9. D. A. Wilson, R. M. Sullivan, *Neuron* **72**, 506–519 (2011).
10. K. Miyamichi *et al*., *Nature* **472**, 191–196 (2011).
11. J. M. Bekkers, N. Suzuki, *Trends Neurosci.* **36**, 429–438 (2013).
12. D. D. Stettler, R. Axel, *Neuron* **63**, 854–864 (2009).
13. M. Ma, *Crit. Rev. Biochem. Mol. Biol.* **42**, 463–480 (2007).
14. J. C. Viemari, M. Bévengut, P. Coulon, G. Hilaire, *J. Neurophysiol.* **91**, 746–758 (2004).
15. J. W. Yang *et al*., *Curr. Opin. Neurobiol.* **53**, 29–34 (2018).
16. S. Moriceau, R. M. Sullivan, *Dev. Psychobiol.* **47**, 230–242 (2005).
17. L. Cai *et al*., *J. Neurosci.* **42**, 4435–4448 (2022).
18. A. H. Leighton, C. Lohmann, *Front. Neural Circuits* **10**, 1–13 (2016).
19. E. de Villers-Sidani, E. F. Chang, S. Bao, M. M. Merzenich, *J. Neurosci.* **27**, 180–189 (2007).
20. J. Shen, M. T. Colonnese, *J. Neurosci.* **36**, 12259–12275 (2016).
21. M. Sonntag, B. Englitz, C. Kopp-Scheinpflug, R. Rübsamen, *J. Neurosci.* **29**, 9510–9520 (2009).
22. M. K. Müller *et al*., *Front. Cell. Neurosci.* **13**, 119 (2019).
23. Y. Sevelinges, R. M. Sullivan, B. Messaoudi, A. M. Mouly, *Learn. Mem.* **15**, 649–656 (2008).
24. H. Soumiya *et al*., *PLOS ONE* **11**, e0158583 (2016).
25. J.-J. Zheng *et al*., *Nat. Neurosci.* **17**, 391–399 (2014).
26. J. M. Fuster, M. Bodner, J. K. Kroger, Association in Neurons of Frontal Cortex, *Nature* **405**, 347–351 (2000).
27. S. R. Gilissen, L. Arckens, *Curr. Opin. Neurobiol.* **67**, 16–25 (2021).
28. A. R. Garner, G. B. Keller, *Nat. Neurosci.* **25**, 98–105 (2022).
29. L. A. Ibrahim *et al*., *Neuron* **89**, 1031–1045 (2016).
30. G. Iurilli *et al*., *Neuron* **73**, 814–828 (2012).
31. A. Renard, E. R. Harrell, B. Bathellier, *Nat. Commun.* **13**, 3830 (2022).
32. N. Uchida, C. Poo, R. Haddad, *Annu. Rev. Neurosci.* **37**, 363–385 (2014).
33. P. Gupta, D. F. Albeanu, U. S. Bhalla, *Nat. Neurosci.* **18**, 272–281 (2015).
34. M. H. Teicher, E. M. Blass, *Science* **198**, 635–636 (1977).
35. P. C. Brunjes, J. R. Alberts, *J. Comp. Physiol. Psychol.* **93**, 548–555 (1979).
36. F. Muscatelli, S. G. Bouret, *Curr. Opin. Neurobiol.* **52**, 165–171 (2018).
37. P. G. Hepper, *Anim. Behav.* **31**, 1177–1191 (1983).
38. T. Toda, H. Kawasaki, *Mol. Brain* **7**, 8 (2014).
39. S. W. Oh *et al*., *Nature* **508**, 207–214 (2014).
40. Y. Ben-Ari, *Nat. Rev. Neurosci.* **3**, 728–739 (2002).
41. J. E. Cometto-Muñiz, W. S. Cain, M. H. Abraham, J. M. R. Gola, *Physiol. Behav.* **67**, 269–276 (1999).
42. R. L. Doty *et al*., *Physiol. Behav.* **20**, 175–185 (1978).
43. D. Krone, M. Mannel, E. Pauli, T. Hummel, *Phytother. Res.* **15**, 135–138 (2001).
44. J. Frasnelli, B. Schuster, T. Zahnert, T. Hummel, *Neuroscience* **142**, 541–546 (2006).
45. J. Frasnelli, B. Schuster, T. Hummel, *Neurosci. Lett.* **468**, 259–263 (2010).
46. J. Frasnelli, T. Hummel, *Int. J. Psychophysiol.* **65**, 177–181 (2007).
47. V. Van Regemorter *et al*., *Curr. Otorhinolaryngol. Rep.* **10**, 421–426 (2022).
48. H. Gudziol, M. Schubert, T. Hummel, *ORL J. Otorhinolaryngol. Relat. Spec.* **63**, 72–75 (2001).
49. J. Frasnelli, B. Schuster, T. Hummel, *Cereb. Cortex* **17**, 370–377 (2007).
50. E. Iannilli, J. Gerber, J. Frasnelli, T. Hummel, *Brain Res.* **1139**, 235–244 (2007).

ACKNOWLEDGMENTS

We would like to thank F. Helmchen and S. Han for the initial support with and access to the behavioral setup and J.-W. Yang

for his contribution in setting up the equipment and analysis for the silicon-probe recording. We also thank K. Otomo, L. Facheris, and A. Cavaccini for help with experiments and analysis. Slide scanner imaging was performed with equipment maintained by the Center for Microscopy and Image Analysis (ZMB), University of Zurich (UZH). **Funding:** This research was supported by the European Research Council (ERC, 679175, to T.K.), the Swiss National Science Foundation (SNSF, 31003A_170037, to T.K.), the UZH URPP AdaBD (to T.K.), and a UZH Candoc Grant (FK-23-031, to L.C.). **Author contributions:** Conceptualization: T.K., L.C., and A.Ô.A. Methodology: L.C., A.D., and A.Ô.A. Investigation: L.C., A.D., and A.Ö.A. Visualization: L.C. Funding acquisition: T.K. and L.C. Project administration: T.K. Supervision: T.K. Writing – original draft: L.C. and T.K. Writing – review and editing: L.C., A.D., A.Ö.A., and T.K. **Competing interests:** The authors declare that they have no competing interests. **Data and materials availability:** All data are available in the main text or the supplementary materials.

SUPPLEMENTARY MATERIALS

science.org/doi/10.1126/science.adn5611
Materials and Methods
Supplementary Text
Figs. S1 to S6
References (*51–68*)
MDAR Reproducibility Checklist

Submitted 15 December 2023; accepted 5 April 2024
10.1126/science.adn5611